Check for updates

ADVANCED MATERIALS
www.advmat.de

Fully Depleted Self-Aligned Heterosandwiched Van Der Waals Photodetectors

Fang Wang, Zhiyi Liu, Tao Zhang, Mingsheng Long, Xiuxiu Wang, Runzhang Xie, Haonan Ge, Hao Wang, Jie Hou, Yue Gu, Xin Hu, Ze Song, Suofu Wang, Qingsong Dong, Kecai Liao, Yubing Tu, Tao Han, Feng Li, Zongyuan Zhang, Xingyuan Hou, Shaoliang Wang, Liang Li, Xueao Zhang, Dongxu Zhao, Chongxin Shan, Lei Shan,* and Weida Hu**

Room-temperature-operating highly sensitive mid-wavelength infrared (MWIR) photodetectors are utilized in a large number of important applications, including night vision, communications, and optical radar. Many previous studies have demonstrated uncooled MWIR photodetectors using 2D narrow-bandgap semiconductors. To date, most of these works have utilized atomically thin flakes, simple van der Waals (vdW) heterostructures, or atomically thin p–n junctions as absorbers, which have difficulty in meeting the requirements for state-of-the-art MWIR photodetectors with a blackbody response. Here, a fully depleted self-aligned MoS_2-BP-MoS_2 vdW heterostructure sandwiched between two electrodes is reported. This new type of photodetector exhibits competitive performance, including a high blackbody peak photoresponsivity up to 0.77 A W^{-1} and low noise-equivalent power of 2.0×10^{-14} W $Hz^{-1/2}$, in the MWIR region. A peak specific detectivity of 8.61×10^{10} cm $Hz^{1/2}$ W^{-1} under blackbody radiation is achieved at room temperature in the MWIR region. Importantly, the effective detection range of the device is twice that of state-of-the-art MWIR photodetectors. Furthermore, the device presents an ultrafast response of ≈4 µs both in the visible and short-wavelength infrared bands. These results provide an ideal platform for realizing broadband and highly sensitive room-temperature MWIR photodetectors.

1. Introduction

A blackbody photoresponse is highly desired in 2D infrared photodetectors which determines their practical applications. State-of-the-art available blackbody response mid-wavelength infrared (MWIR) photodetectors are fabricated using HgCdTe,[1–4] PbSe,[5,6] and InSb.[7] However, these photodetectors need to operate at cryogenic temperatures to minimize thermally generated dark current and noise, which not only increases the overall system size and cost but also limits their wide application. Therefore, developing next-generation MWIR photodetectors that are suitable for chip-scale integration and operation at room temperature is urgent. Fortunately, the discovery of 2D narrow-bandgap semiconductors such as black phosphorus (BP), Te, $PdSe_2$, and $PtSe_2$, with high carrier mobility and strong infrared light absorption has opened up new opportunities

F. Wang, Z. Liu, M. Long, X. Wang, J. Hou, X. Hu, Z. Song, S. Wang, Q. Dong, K. Liao, Y. Tu, T. Han, F. Li, Z. Zhang, X. Hou, S. Wang, L. Li, L. Shan
Information Materials and Intelligent Sensing Laboratory of Anhui Province
Key Laboratory of Structure and Functional Regulation of Hybrid Materials of Ministry of Education
Institutes of Physical Science and Information Technology
Anhui University
111 Jiu Long Road, Hefei 230601, China
E-mail: longms@ahu.edu.cn; lshan@ahu.edu.cn

F. Wang, T. Zhang, R. Xie, H. Ge, H. Wang, Y. Gu, W. Hu
State Key Laboratory of Infrared Physics
Shanghai Institute of Technical Physics
Chinese Academy of Sciences
Shanghai 200083, China
E-mail: wdhu@mail.sitp.ac.cn

X. Zhang
College of Physical Science and Technology
Xiamen University
Xiamen 361005, China

D. Zhao
State Key Laboratory of Luminescence and Applications
Changchun Institute of Optics
Fine Mechanics and Physics
Chinese Academy of Sciences
3888 Dongnanhu Road, Changchun 130021, China

C. Shan
Henan Key Laboratory of Diamond Optoelectronic Materials and Devices
School of Physics and Engineering
Zhengzhou University
Zhengzhou 450001, China

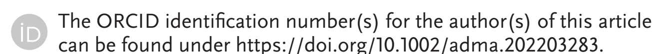
The ORCID identification number(s) for the author(s) of this article can be found under https://doi.org/10.1002/adma.202203283.

DOI: 10.1002/adma.202203283

 © 2022 Wiley-VCH GmbH

15214095, 2022, 39, Downloaded from https://onlinelibrary.wiley.com/doi/10.1002/adma.202203283 by Cas-Changchun Institute Of Optics, Fine Mechanics And Physics, Wiley Online Library on [06/02/2023]. See the Terms and Conditions (https://onlinelibrary.wiley.com/terms-and-conditions) on Wiley Online Library for rules of use; OA articles are governed by the applicable Creative Commons License

for uncooled MWIR detection[8–16] with a thinner absorber and lower thermal noise.[17] In particular, 2D layered crystals without dangling bonds can reduce the noise generated by generation-recombination and avoid problems such as lattice mismatch.[18] To realize high photoresponsivity, many strategies have been used to enhance light absorption, such as waveguide-integrated [19–21] BP photodetectors, induced plasmonic structures,[22] and Fabry–Pérot cavities.[23] Due to the narrow direct bandgap property, the BP phototransistor exhibits excellent performance in MWIR photodetection. Under an MWIR wavelength of 3.39 μm, a photoresponsivity of 82 A W^{-1} was demonstrated.[23] The detection spectral range of BP could be broadened by atom doping and external voltage application. The bandgap could be tuned down to 0.15 eV (corresponding to 8.3 μm) by replacing 83% of the phosphorus atoms with arsenic atoms (b-$As_{0.83}P_{0.17}$), which covers the long-wavelength infrared (LWIR) spectral range of the 8–14 μm atmosphere window.[25,26] By applying a vertical electric field, the detection spectral range of the BP phototransistor could be broadened to 7.7 μm.[27] To date, only a few photodetectors based on 2D materials exhibit a blackbody response, such as BP and black arsenic phosphorus (b-AsP) phototransistors,[28] BP-MoS_2 heterostructures,[29] BP/MoS_2/graphene unipolar barrier photodetectors (p–B–p),[30] and low-dimensional tellurium.[31] The blackbody photoresponse is still a major challenge since it requires not only high sensitivity but also fast speed which is difficult to simultaneously meet for most photodetectors based on 2D materials. An uncooled blackbody response was demonstrated based on BP and b-$As_{0.91}P_{0.09}$ during operation in photoconductive (PC) mode, with a high blackbody peak specific detectivity up to $\approx 6 \times 10^{10}$ cm $Hz^{-1/2}$ W^{-1}.[28] However, the BP and Te photodetectors operating in PC mode suffer from a high dark current due to their narrow bandgap property. The dark current could be depressed to 15 pA by designing unipolar barriers (n–B–n and p–B–p) to block the majority carriers.[30] The most widely used strategy to suppress the dark current is to fabricate 2D material p–n junctions to induce a built-in electric field. Due to the potential barriers at the interface of the vdW heterostructures or in the contact region with the metal electrodes, the photocurrent is also depressed especially in the MWIR range, which remains a great issue.

To realize high-performance MWIR photodetectors, light absorption should be enhanced, photocarrier separation and collection efficiency should be strengthened, and high dark current and noise power density should be suppressed. Here, we propose a fully depleted self-aligned MoS_2–BP–MoS_2 (MPM) vdW heterojunction setting on a bottom mirror electrode to enhance light absorption. For the self-aligned top electrode contact with the MoS_2 flakes, 8 nm Bi and 2 nm Au were used to obtain good ohmic contact.[32] The self-aligned lateral electrode deposited on BP was used to shorten the lateral transport distance for fast photocarrier collection. The vertical MPM vdW heterojunction was manufactured using a dry-transfer technique.[33] The built-in electric field effectively suppresses the high dark current. In this vertical MPM vdW heterojunction, the infrared absorber layer of BP is fully depleted, allowing the photocarriers to be effectively separated. The transmission distance for photocarriers in the vertical direction, which contribute to the photocurrent, is only tens of nanometres. This short vertical distance can result in fast photoresponse and a high photocurrent gain, thereby achieving a high-performance uncooled MWIR photodetector with a high blackbody peak photoresponsivity up to 0.77 A W^{-1}, low noise-equivalent power of 2.0×10^{-14} W $Hz^{-1/2}$, and a peak specific detectivity D^* up to 8.61×10^{10} cm $Hz^{-1/2}$ W^{-1} under 1073 K blackbody radiation. The effective detection range (proportion of the spectral specific detectivity higher than 75% of the peak D^*) of our device is up to 75% which is twice that of other MWIR photodetectors.

2. Results and Discussion

A schematic diagram of the metal-mirror-enhanced MoS_2/BP/MoS_2 heterojunction is shown in **Figure 1**a. The device was obtained by sandwiching a BP (p-type) flake between two MoS_2 (n-type) flakes via dry transfer technology. Here, the bottom electrode of the MPM vdW heterostructure was used to reflect the light and shorten the photocarrier transport distance. The fabrication process of the self-aligned MoS_2/BP/MoS_2 vdW photodetector is shown in Figure S1 (Supporting Information). The details are presented in Note 1 (Supporting Information). For the top electrode, a process involving self-alignment and deposition of 8 nm Bi and 2 nm Au was adopted to realize ohmic contact with MoS_2 and shorten the lateral transport distance. The reflection top and bottom electrodes are used to increase the distance of the light transport to enhance light absorption as shown in Figure S2a (Supporting Information). According to the light absorption law, the absorption spectra can be expressed as $A(\lambda) = 1 - e^{-\alpha(\lambda)d}$, where $\alpha(\lambda) = 4\pi k/\lambda$ is the light absorption coefficient, $k = \sqrt{\left(\sqrt{\varepsilon_2^1 + \varepsilon_2^2} - \varepsilon_1\right)/2}$ is the index of refraction, and ε_1 and ε_2 are the real and imaginary parts of the dielectric function, respectively (see Note 2, Supporting Information). When light is incident on the device, the light absorption can be considerably enhanced after multiple reflections, as sketched in Figure S2a (Supporting Information). We further proved the ultrawide spectral response source of the device through finite element electromagnetic (2D EM) simulation. The dielectric function of the materials in the simulation is referred to in previous works.[29,34,35] For direct bandgap BP, the light absorption of the 20 nm film is 8%, which corresponds to 0.4% per nanometer.[36] The energy-dispersive X-ray spectroscopy (EDS) mapping of Au, Mo, P, Mo, and Au for the Au–MoS_2/BP/MoS_2–Au cross-section shown in Figure S2b (Supporting Information) and the Raman spectra of the BP, MoS_2, and BP–MoS_2 junction area in Figure S4a and Note 3 (Supporting Information) indicate that high-quality vdW heterojunctions are obtained. For the photovoltaic response, photogenerated electrons are dragged in two opposite directions of the top and bottom MoS_2 films by the built-in electric field of this MPM device and are collected by a metal electrode. The photogenerated holes are dragged to BP and then collected by another metal electrode. The two parallel p–n junctions can shorten the photocarrier transmission distance, and the two mirror electrodes act as a light reflector to increase the light absorption, which can also enhance the photocarrier collection efficiency. The energy band alignment of the MoS_2, BP, and MoS_2 before contact is presented in Figure 1b. During the MoS_2 contact with BP, the

© 2022 Wiley-VCH GmbH

15214095, 2022, 39, Downloaded from https://onlinelibrary.wiley.com/doi/10.1002/adma.202203283 by Cas-Changchun Institute Of Optics, Fine Mechanics And Physics, Wiley Online Library on [06/02/2023]. See the Terms and Conditions (https://onlinelibrary.wiley.com/terms-and-conditions) on Wiley Online Library for rules of use; OA articles are governed by the applicable Creative Commons License

15214095, 2022, 39, Downloaded from https://onlinelibrary.wiley.com/doi/10.1002/adma.202203283 by Cas-Changchun Institute Of Optics, Fine Mechanics And Physics, Wiley Online Library on [06/02/2023]. See the Terms and Conditions (https://onlinelibrary.wiley.com/terms-and-conditions) on Wiley Online Library for rules of use; OA articles are governed by the applicable Creative Commons License

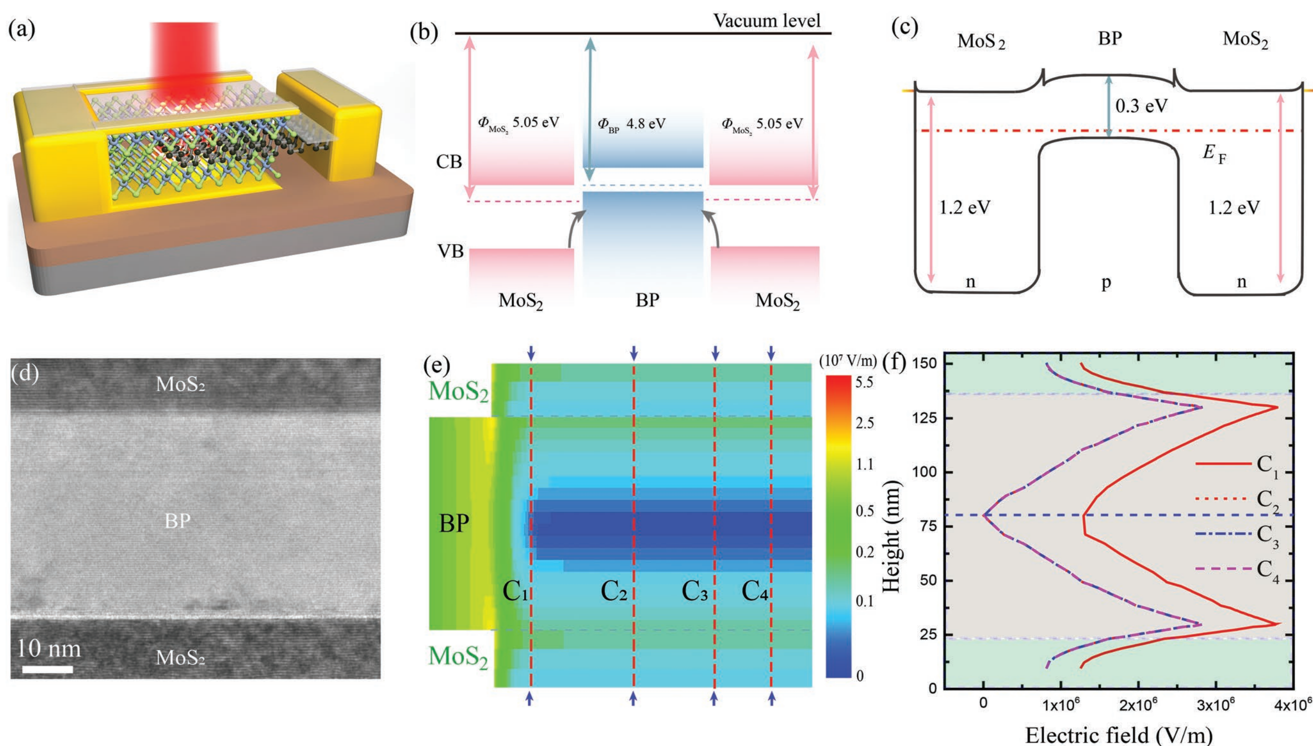

Figure 1. MPM vertical heterostructure photodetector. a) Schematic of the MoS_2–BP–MoS_2 self-aligned hetero-sandwiched vdW photodetector. b) Band structure of the BP, MoS_2, and BP, respectively before contact. c) Band aliment of the MPM heterostructure in equilibrium. d) Cross-sectional TEM image of the heterostructure. e) Simulated vertical potential distribution of the MPM device under zero bias. f) Built-in electric field profiles along the vertical directions marked in (e).

electrons were transferred to MoS_2, and holes were transferred to BP that the work function of MoS_2 ≈5.05 eV[37] is higher than that of BP ≈ 4.8 eV.[38] The energy band structure of the MoS_2–BP–MoS_2 heterostructure device under equilibrium is shown in Figure 1c. The band structures of these MPM double junctions with MoS_2 flakes of different thicknesses are considered to possess symmetric structures because two MoS_2 flakes of such thicknesses have the same bandgap as the bulk form.[39] The light absorption edge of these MPM double junctions depends on the bandgap of BP. The depletion region is crucial for a photovoltaic response. The high-resolution transmission electron microscopy (TEM) image of the cross-section of the MoS_2/BP/MoS_2 heterojunction in Figure 1d and the zoomed-in TEM image of BP-MoS_2 in Figure S2c (Supporting Information) show that the two interfaces between MoS_2 and BP are very clean, without any contamination during device fabrication. To observe the depletion region of the MPM device, the spatial potential distribution was simulated by the finite element method with Sentaurus TCAD software. The vertical potential distribution at the cross-section of the MPM device is presented in Figure 1e. The electric field penetrates the entire device, indicating that the device is fully depleted in the vertical direction. Built-in electric field profiles along the vertical direction, which were cut along the red dashed lines C_1 to C_4 in Figure 1e, are presented in Figure 1f. Vertical electric field peaks up to 3.8×10^6 V m^{-1} were observed at the BP near the top and bottom p–n junctions. To investigate whether the BP is fully depleted in these devices, we further carried out the Kelvin probe force microscopy (KPFM) and atomic force microscopy (AFM) measurements, as shown in Figure S3a (Supporting Information). The step between the top MoS_2 and the BP is very sharp, as shown in Figure S3b (Supporting Information). The contact potential difference (CPD) between MoS_2 and the BP flakes spacing along the lateral direction is ≈1 µm, as shown in Figure S3c (Supporting Information), indicating the depleted distance is much longer than the thickness of the BP, which further verified that the BP was depleted.

Then we studied the optoelectrical properties of the double p–n junction device. The optical micrograph of a typical self-aligned MPM vdW heterojunction is presented in Figure S4b (Supporting Information), and the thickness of different layers in the heterojunction was checked by atomic force microscopy (AFM), as shown in Figure S4d–S4f (Supporting Information). The output curves with and without illumination are presented in **Figure 2**a. In the dark, rectification behavior is observed, indicating that a built-in electric field is formed. The incident light power is 1.86 µW for an MWIR laser (3300 nm). When the light is incident on the device, the current significantly increases. We then systematically investigated the photovoltaic response in the MWIR range and measured the temporal photovoltaic response under various light powers of a 3590 nm laser, as shown in Figure 2b. The light power dependence of the photovoltaic response from 1650 to 3951 nm is presented in Figure S5 (Supporting Information). The current sharply increases/decreases when the incident light is turned on/off, indicating that the photoresponse is very fast. We extracted the

 © 2022 Wiley-VCH GmbH

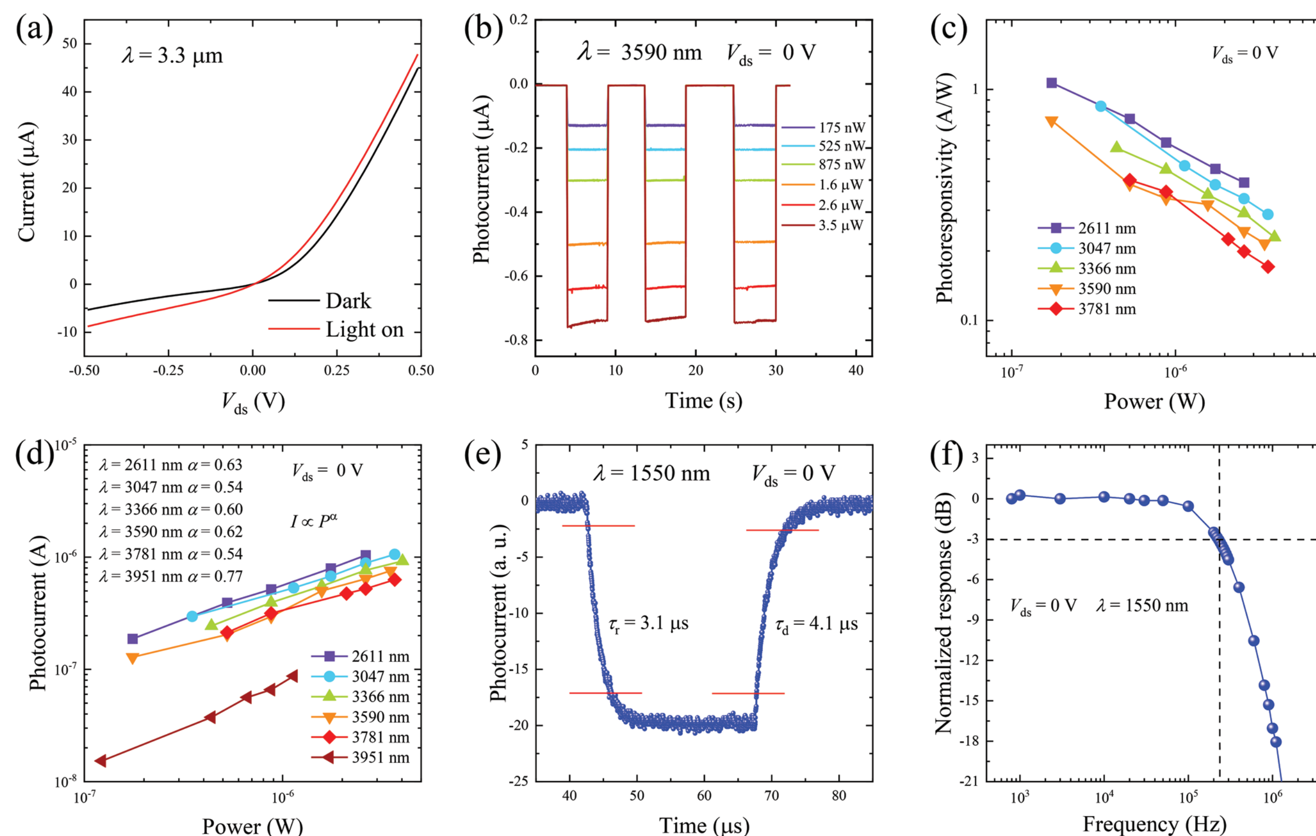

Figure 2. Photoresponse of a typical MPM device in the infrared region. a) *I–V* curves of a typical MPM device with and without illumination. b) Time-resolved photovoltaic response under various incident light powers (3590 nm laser). c) Incident light power dependence of the *R* of typical MoS_2/BP/MoS_2 vdW heterojunction photodetectors in the MWIR region at V_{ds} = 0 V in ambient air. d) A sublinear power dependence of the photocurrents under MWIR ($\alpha < 1$) at zero bias. e) Rise and decay times of the MPM device at a bias of 0 V under a 1550 nm laser. f) Normalized photoresponse as a function of the modulated frequency under 1550 nm laser at a bias of 0 V.

photocurrent $I_P = I_{on} - I_{off}$ and calculated the photoresponsivity $R = I_P/P_{in}$, where P_{in} is the light power incident on the device. Another figure-of-merit, the external quantum efficiency (EQE), is used to evaluate the performance of photodetectors, which is defined as the ratio of the number of photogenerated carriers (N_I) to the number of incident photons (N_P). EQE can be calculated by EQE = $N_I/N_P = hcR/e\lambda$. Figure 2c shows the extracted light power dependence of *R* under MWIR from 2611 to 3781 nm. The photovoltaic *R* and EQE for a 3590 nm laser reach ≈0.73 A W^{-1} and 25.3% at 175.1 nW. As the light power increases to 3.5 μW, *R*, and EQE decrease to 0.21 A W^{-1} and 7.4%, respectively. All responsivities show a decreasing trend as the illumination power increases. EQE values ranging from 2.3% to 50.7% are realized at zero bias in the MWIR range.

Then we measured the photoresponse from visible to short-wavelength infrared (SWIR). In the SWIR range, we also measured the photoresponse near the optical communication SWIR wavelength of 1650 nm, and 1310 nm. The extracted photocurrent as a function of light power in the MWIR range is plotted in Figure 2d, and visible and SWIR are presented in Figure S6 (Supporting Information). Sublinear light power-dependent photocurrent behavior ($I_P \propto P^{\alpha}$, $\alpha < 1$) is observed. The value α ranges from 0.98 to 1.0 in the visible range, range from 0.88 to 0.98 in the SWIR range, and from 0.54 to 0.77 in the MWIR range. This sublinear light power dependence behavior was observed widely in previous works[40,41] in 2D materials. The sublinear behavior indicates that trap centers are present in the channel materials which can induce photogain. When the device operates under lighter power, most of the trap states (of the minority carrier) are filled. In this condition, the further increased light power cannot effectively increase photogain and the recombination probability increased, causing the fall in responsivity.[42] The smaller the value of α is, realizing the higher photogain due to long decay time and more trap centers participate in the photoresponse.[43] In our device, the small value of α was realized in MWIR, the long wavelength range. In the MWIR range, due to the long lifetime of the trap states, the photoresponse time is much longer than that in the short-wave range. This behavior of α value correlated to response time, trap density,[43] and gate voltage[41] was observed. A photovoltaic responsivity of ≈0.61 A W^{-1} and an EQE of ≈45.8% are realized under a 1650 nm laser.

In the visible range, the photoresponse to a 637 nm laser was investigated. We systematically measured the incident light power dependence photoresponse. The *I–V* curves with various incident light powers of 637 nm laser and without light are presented in Figure S7a (Supporting Information). The incident light power ranges from 1.9 to 91.5 μW. Then we extracted the

 © 2022 Wiley-VCH GmbH

15214095, 2022, 39, Downloaded from https://onlinelibrary.wiley.com/doi/10.1002/adma.202203283 by Cas-Changchun Institute Of Optics, Fine Mechanics And Physics, Wiley Online Library on [06/02/2023]. See the Terms and Conditions (https://onlinelibrary.wiley.com/terms-and-conditions) on Wiley Online Library for rules of use; OA articles are governed by the applicable Creative Commons License

light-power-dependent open-circuit voltage (V_{oc}) and short-circuit current (I_{sc}). The V_{oc} versus the incident light power density is plotted in Figure S7b (Supporting Information). The optical image of the metal-mirror-enhance MPM device is shown in inset of Figure S7b (Supporting Information). As the bias at the open-circuit voltage, a balance between photogeneration (Gr $\propto P_I$) and interlayer recombination (Re) rates. The recombination rate can be expressed as the empirical equation Re $= fn^{\beta}$, where f is a prefactor determined by the actual recombination process, β is the recombination order, and $n = p$ is the electron density. $\beta = 1$ for monomolecular (Shockley–Read–Hall, SRH) recombination and $\beta = 2$ for bimolecular (Langevin) recombination.[44,45] For p–n junction the $qV_{oc} = E_g + k_BT\ln(np/N_c^2)$,[45] the parameter β can be obtained at Gr = Re from the following express:

$$\frac{dV_{oc}}{d\ln P_I} = \frac{2}{\beta}\frac{k_BT}{q} \tag{1}$$

where E_g is the bandgap, N_c is the effective density of states, and k_B is the Boltzmann constant. The $\beta = 1.46$ was extracted by fitting the experimental data as shown in Figure S7b (Supporting Information) (red dashed line), indicating the interlayer recombination is dominated by the SRH process and further evidence of the existence of trap states in this device. The short-circuit current as a function of incident light power is presented in Figure S7c (Supporting Information). The I_{sc} increased linearly as the light power increased. No tendency of saturation was observed over the measured range of optical power. We also measured the photoresponse in the visible range of 637 nm at a bias of 2 V and 520 nm at a bias of 1 V. The response time of 637 nm at a bias of 0 V is presented in Figure S7d (Supporting Information) with $\tau_r = 4.4$ µs and $\tau_d = 3.6$ µs. At lower power intensity, there are sufficient available carrier trap centers, which lead to a long photocarrier lifetime τ_L. At $V_{ds} = 2$ V, the photoresponsivities tend to saturate at low power. At higher power intensity, the trap centers saturate, and the recombination rate increases due to more free electrons and holes, resulting in reduced photoresponsivity. The incident light power dependence of the photocurrent can be well fitted by the Hornbeck-Haynes formula[24,46]:

$$I_P = e\eta\left(\frac{\tau_L}{\tau_T}\right)\frac{F}{1+\left(F/F_0\right)} \tag{2}$$

where η is the light absorption efficiency, τ_T is the transit time, and F and F_0 in units of s^{-1} are the photon absorption rates at unsaturated and saturated trap centers, respectively. The incident light power on the device can be expressed as $P_{in} = h\nu F/\eta = hcF/(\lambda\eta)$. The photoresponsivity can be derived from Equation (1):

$$R = \frac{I_P}{P_{in}} = \frac{e\lambda\eta^2}{hc}\left(\frac{\tau_L}{\tau_T}\right)\frac{1}{1+\left(F/F_0\right)} \tag{3}$$

The R at a 2 V bias could be well fitted by Equation (3), shown as the olive dashed line in Figure S7e (Supporting Information), indicating that the photogating effect dominates the photoresponse. The light power dependence R and EQE of 520 nm laser at a 1 V bias, as shown in Figure S7f (Supporting Information). R of up to 124.3 A W^{-1} and a corresponding EQE of up to 29 648.7% are obtained at 520 nm. A high photogain is observed in 2D semiconductors and their heterostructures due to the trap states[24] and charge transfer at the interface.[47,48] Under high power intensity ($P_I > 30$ nW), the photoresponsivities are higher than the fitted values. In this range, the trap centers are saturated, and the traditional PC effect plays a major role in the photocurrent.[24] A fast photoresponse is a crucial figure of merit for a photodetector. Thus, we measured the response speed at a 0 V bias under a 1550 nm laser. The rise time ($\tau_r = 3.1$ µs), i.e., the time for the photocurrent to increase from 10% to 90%, and the decay time ($\tau_d = 4.1$ µs), i.e., the time for the photocurrent to decay from 90% to 10%, were obtained, as shown in Figure 2e. Furthermore, the −3 dB cutoff frequency of 0.23 MHz was obtained, which was extracted from the frequency dependence photoresponse under 1550 nm laser at the modulation frequency when the signal drops to 70% of its initial value, as shown in Figure 2f. The raising time τ_r could be estimated using the equation $\tau_r = 0.35/f\,(-3\text{ dB})$ to be 1.5 µs, a slit shorter than the response time measurement.

To investigate the wavelength-dependent photoresponse of such MPM devices, we measured the photoresponse while varying the wavelength of the excitation light. **Figure 3**a shows R and EQE versus the incident light wavelength at $V_{ds} = 0$ V. From the visible to MWIR spectral range (405–3951 nm), the PV responsivity ranges from 0.12 to 1.06 A W^{-1}. EQE as a function of wavelength is shown on the right y-axis of Figure 3a. As the wavelength increases, EQE slowly decreases from 66.8% to 3.9%.

To realize high detectivity, both high photoresponsivity and low current noise power density are required. We measured the photoresponsivity at a low bias of 1 mV. The wavelength dependence of the photoresponsivity and EQE are presented in Figure S8. As the wavelength of the light increases (the energy of the photons decreases) from 0.405 µm to 1.65 µm, the photoresponsivity slowly increases from 0.52 A W^{-1} to 0.79 A W^{-1}. Then, R decreased slowly to 0.57 A W^{-1} as the wavelength increased to 3.366 µm and then sharply decreases to 0.9 A W^{-1} as the wavelength increased from 3.95 µm. The rapid decrease in the photoresponse occurs at the absorption edge of BP, corresponding to a bandgap of ≈0.3 eV.

Finally, we investigated the sensitivity of the MPM heterostructure devices. The two most important figures of merit, the noise equivalent power (NEP) and the specific detectivity (D^*) are used to evaluate the minimum light power that a device can pick up from the noise. To extract the NEP and D^*, we measured the current noise power spectra at different biases. Figure 3b presents the current noise power spectra at 0 V, 1 mV, 10 mV, and 100 mV. At low bias, $V_{ds} = 0$ V, the noise power densities are much smaller than those at other biases. From the current noise spectra at 0 V, flicker noise (1/f) dominates the low-frequency (1 Hz-1 kHz) noise power contribution which originates from the fluctuation of carriers being trapped and de-trapped by the defect centers. When the frequency is above 1 kHz, the current noise power density becomes independent of frequency (white noise). Two types of white noise, shot noise and Johnson noise (also known as thermal noise), may dominate the noise contribution in the higher frequency

© 2022 Wiley-VCH GmbH

15214095, 2022, 39, Downloaded from https://onlinelibrary.wiley.com/doi/10.1002/adma.202203283 by Cas-Changchun Institute Of Optics, Fine Mechanics And Physics, Wiley Online Library on [06/02/2023]. See the Terms and Conditions (https://onlinelibrary.wiley.com/terms-and-conditions) on Wiley Online Library for rules of use; OA articles are governed by the applicable Creative Commons License

15214095, 2022, 39, Downloaded from https://onlinelibrary.wiley.com/doi/10.1002/adma.202203283 by Cas-Changchun Institute Of Optics, Fine Mechanics And Physics, Wiley Online Library on [06/02/2023]. See the Terms and Conditions (https://onlinelibrary.wiley.com/terms-and-conditions) on Wiley Online Library for rules of use; OA articles are governed by the applicable Creative Commons License

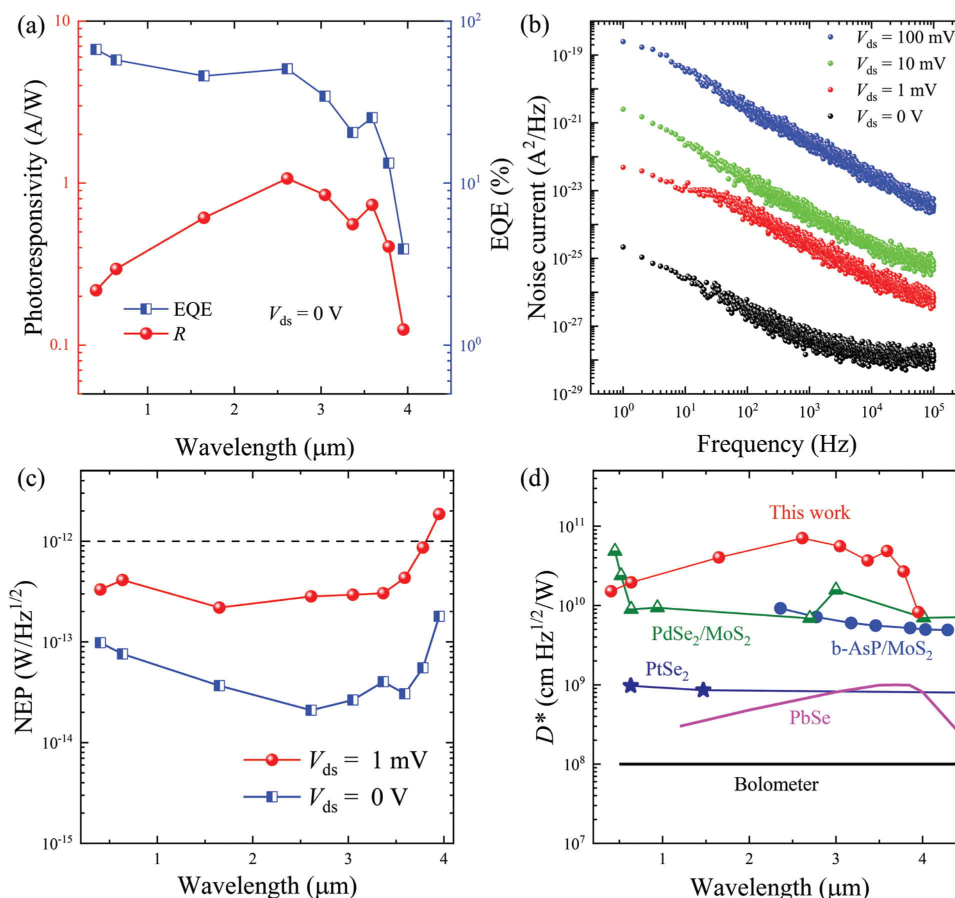

Figure 3. Broadband photoresponse from the visible to MWIR region of a typical MPM device. a) Wavelength dependence of the photoresponsivity and EQE at V_{ds} = 0 V. b) Current noise power spectra of the MPM device at V_{ds} = 0 V, 1 mV, 10 mV, and 100 mV for the black light circles, the red squares, green triangles, and the blue triangles, respectively. c) Wavelength dependence of NEP at V_{ds} = 0 V (blue solid squares), and V_{ds} = 1 mV (red solid circles). d) Wavelength and bias dependence of the specific detectivity D^* of the MPM vdW photodetector, state-of-the-art other photodetectors based on 2D materials, and commercially available infrared photodetectors.

range. Shot noise can be evaluated by $\langle i_n^2 \rangle = 2eI_d\Delta B$,[49] where ΔB is the bandwidth. At V_{ds} = 1 mV, I_d = 57.2 nA, and ΔB = 1 Hz, $\langle i_n^2 \rangle = 1.83 \times 10^{-26}$ A² Hz⁻¹, which is very close to the measured value 2.99×10^{-26} A² Hz⁻¹. The Johnson noise level can be expressed as $\langle i_n^2 \rangle = 4k_BTB/R_0$, where k_B is the Boltzmann constant, and R_0 is the device resistance. The Johnson noise $\langle i_n^2 \rangle = 9.4 \times 10^{-25}$ A² Hz⁻¹ is obtained at ΔB = 1 Hz, and R_0 = 17.4 kΩ for the 1 mV bias, and T = 300 K, which is one order of magnitude higher than the shot noise level. In the current noise spectrum at a 1 mV bias, when the frequency is higher than 300 Hz, the current noise power density is lower than that of Johnson noise $\langle i_n^2 \rangle = 9.4 \times 10^{-25}$ A² Hz⁻¹. The Johnson noise doesn't the major contributes at 1 mV bias. At a higher bias, the Johnson noise is the major contributor since a higher bias drives a higher current and generates more heat. The NEP could be calculated by NEP = i_n/R.[49] From the measured current noise power spectra, we calculated $\langle i_n^2 \rangle$ using the formula $\langle i_n^2 \rangle = \frac{1}{B}\int_0^B S_n(f)\mathrm{d}f$. Then we calculated the NEP at 0 V, and 1 mV bias, as shown in Figure 3c. The NEP at zero bias from 0.405 μm to 3.95 μm shows a slight fluctuation from 0.09 pW Hz$^{-1/2}$ to 0.18 pW Hz$^{-1/2}$, indicating that this MPM device can distinguish a weak signal of 0.18 pW from noise when operating under the PV model. The NEP at a 0 V bias is lower than that at a 1 mV bias, indicating that the device operates at a low bias with high performance. At higher bias, high R can be realized, but the current noise power density also significantly increases. Thus, a low signal-to-noise ratio will appear at a high bias. The NEP at 1 mV is lower than 1.8 pW Hz$^{-1/2}$ from 0.405 μm to 3.95 μm. To compare the performance of such MPM MWIR photodetectors, we summarize the figures of merit for 2D material MWIR photodetectors in Table 1 (Supporting Information). The lower NEP indicates that the device has an excellent capability to distinguish between signal and noise, which can be realized at high photoresponsivity and low current-noise power density. Due to the high photocarrier collection efficiency, such a dual p–n junction configuration can suppress the dark current noise and realize high photoresponsivity. After evaluating the performance of the MPM double p–n junction devices by the NEP, we can obtain another important figure of merit, the specific detectivity D^*. The formula $D^* = (AB)^{1/2}R/i_n$ is used to calculate the specific detectivity, where A is the active area of the device, and B is the measurement bandwidth. In Figure 3d, the wavelength-dependent specific

detectivities at different biases are presented. For the PV response, D^* shows slight fluctuations from 7.06×10^{10} to 8.26×10^9 cm Hz$^{1/2}$ W^{-1}. The D^* from the visible to MWIR region (0.405–3.951 µm) shows a slight increase from 1.51×10^{10} cm Hz$^{1/2}$ W^{-1} to 7.06×10^{10} cm Hz$^{1/2}$ W^{-1}, followed by a slow decrease to 4.86×10^{10} cm Hz$^{1/2}$ W^{-1}. Then rapidly drop to 8.26×10^9 cm Hz$^{1/2}$ W^{-1} as the wavelength increases from 3.59 µm to 3.951 µm. The sharp decrease in D^* stems from the rapid decrease in R near the BP absorption edge. The D^* versus wavelength curves of our photodetector and state-of-the-art MWIR photodetectors are shown in Figure 3d. The D^* of our device is better than that in the previous literatures, including those for $PtSe_2$, $PdSe_2$–MoS_2, and b-AsP-MoS_2 in the MWIR region, as well as than that of commercial state-of-the-art bulk PbS (PC, 295 K) and bolometer photodetectors.

Notably, this MPM vdW heterostructure photodetector shows a photoresponse under blackbody radiation at room temperature. We measured the blackbody radiation photoresponse of the MPM vdW photodetector at various blackbody temperatures. To check if the major radiation power and dominant wavelength (λ_m) are covered by the absorption range of the device, the blackbody radiation intensity versus wavelength curves for various blackbody temperatures from 600 K to 1173 K are presented in Figure S9a (Supporting Information). The λ_m marked by the red dashed line is located at the absorption edge of BP when the blackbody temperature is raised to 700 K. To obtain more blackbody radiation power in the absorption region of the MPM device, we measured the blackbody response starting from 1073 K. A Fourier transform infrared spectrometer was used to measure the relative response spectrum of the MPM devices. Figure S9b (Supporting Information) presents the relative response spectrum for the background at room temperature, which was obtained using an internal deuterated triglycine sulfate (DTGS) photodetector. Normalized relative spectral response $R(\lambda)$ of the n–p–n vdW photodetector enhanced by sandwiched metal mirrors under blackbody illumination is shown in **Figure 4**a. It presents an ultrawide spectral response, which is attributed to the absorption of BP (≈3.5 µm), the resonance of upper and lower metal reflectors in the MPM region (≈1.3 µm), and the top electrode-induced resonance in the BP

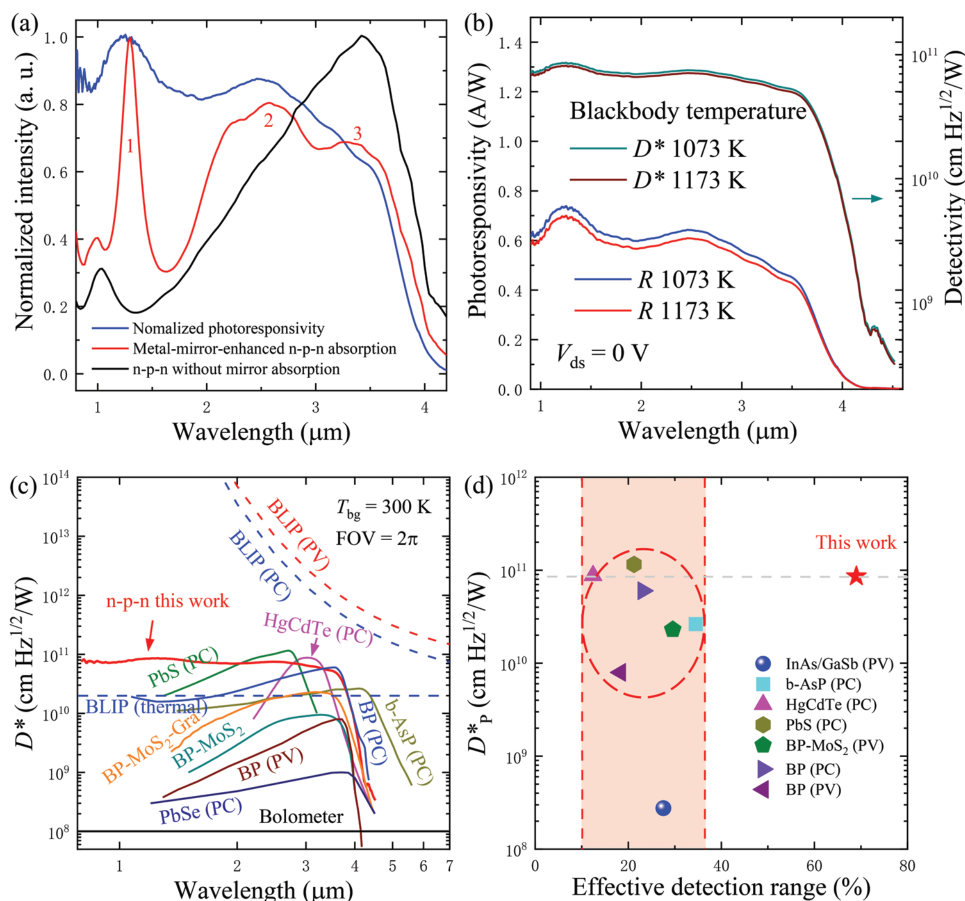

Figure 4. Blackbody response of typical MPM vdW photodetectors enhanced by sandwiched metal mirrors. a) Normalized relative spectral response of the n–p–n vdW photodetector under blackbody illumination (the blue line) and simulated normalized absorption of the n–p–n device with a metal mirror (the red line) and without a metal mirror (the dark line). b) Broadband spectral photovoltaic responsivity of the MPM device under 1053 K (blue line) and 1173 K (red line) blackbody radiation, the left axis. Temperature and wavelength dependence of the specific detectivity D^* of a typical MPM vdW heterostructure photodetector, the right axis. c) Spectral specific detectivity of the MPM vdW heterostructure photodetector, other MWIR photodetectors based on 2D materials, and commercially available infrared photodetectors. d) Peak specific detectivity and effective detection range of MWIR photodetectors.

© 2022 Wiley-VCH GmbH

15214095, 2022, 39, Downloaded from https://onlinelibrary.wiley.com/doi/10.1002/adma.202203283 by Cas-Changchun Institute Of Optics, Fine Mechanics And Physics, Wiley Online Library on [06/02/2023]. See the Terms and Conditions (https://onlinelibrary.wiley.com/terms-and-conditions) on Wiley Online Library for rules of use; OA articles are governed by the applicable Creative Commons License

region (≈2.6 µm). This excellent optical manipulation effect is proved with the finite element method electromagnetic (2D EM) simulation, where the sandwiched resonance structure is extracted from the optical image of the fabricated device. Figure S9c gives the blackbody responsivity at zero bias and small bias voltage with the blackbody temperature of 1073 K and 1173 K. The radiation powers incident on the device were calculated using the approximate formula in this method. The photoresponsivity fluctuates from 0.29 A W^{-1} to 0.32 A W^{-1} as the bias varies from −10 mV to 10 mV. We calculated the blackbody peak photoresponsivity $R_P(T)$ with the blackbody responsivity $R_b(T)$ and g factors, which are extracted from the relative spectral response $R(\lambda)$.

$$g(T) = \frac{R_b}{R_P} = \frac{D_b^*}{D_P^*} = \frac{\int_0^\infty R(\lambda)\Phi(T,\lambda)\mathrm{d}\lambda}{\int_0^\infty \Phi(T,\lambda)\mathrm{d}\lambda} \tag{4}$$

where $\Phi(T,\lambda)$ is the blackbody radiant power distribution. With the blackbody responsivity formula:

$$R_b(T) = \frac{\int_0^\infty R_I(\lambda)\Phi(T,\lambda)d\lambda}{\int_0^\infty \Phi(T,\lambda)d\lambda} = R_P(T)\frac{\int_0^\infty R(\lambda)\Phi(T,\lambda)d\lambda}{\int_0^\infty \Phi(T,\lambda)d\lambda} \tag{5}$$

we can acquire the blackbody peak photoresponsivity $R_P(T) = R_b(T)/g$. Combination with the blackbody radiant power distribution $\Phi(T,\lambda)$ and normalized relative spectral response $R(\lambda)$ in Figure 4a. The g factors of 0.39 and 0.44 were obtained at the blackbody temperatures of 1073 K and 1173 K, respectively. As a result, the blackbody peak photoresponsivity at 1073 K and 1173 K were 0.77 A W^{-1} and 0.73 A W^{-1}. The blackbody response spectrum is presented in Figure 4b on the left y-axis. The cutoff wavelength λ_c = 3.66 µm is extracted as the photoresponsivity drops by 50%. A peak specific detectivity up to 8.61×10^{10} cm Hz$^{1/2}$ W^{-1} is obtained under 1073 K blackbody radiation, as shown in Figure 4b (the right y-axis). The D^* of our MPM vdW heterostructure under blackbody radiation is higher than those of many other commercially available and literature-reported MWIR photodetectors, as shown in Figure 4c. The performance of state-of-the-art MWIR photodetectors is summarized in Table 1 (Supporting Information). Notably, our MPM device shows excellent performance in the SWIR range. For the state-of-the-art MWIR photodetectors, the photoresponsivity and specific detectivity sharply drop as the wavelength deviates from the peak wavelength, as shown in Figure S10 (Supporting Information). The effective detection range is defined as the ratio of the spectral range with a D^* higher than 70% of the peak D^* to the full detection range. To compare the detection ranges of different MWIR photodetectors, the peak D^* and effective detection range was extracted, as shown in Figure 4d. The effective detection range of this MPM photodetector is up to 75%, which is much larger than those of other commercially available and 2D-based MWIR photodetectors, ranging from 10% to 35%, marked by the red dashed circle. Our photodetector shows high D^* (from the SWIR to MWIR region) and broad spectral detection capability and has great potential application in infrared imaging. It is worth mentioning that this metal-mirror-enhanced MPM heterostructure device sealed by a PMMA layer exhibits good stability in ambient air. As shown in Figure S11 (Supporting Information), the performance of the device didn't decrease when the device was exposed to air for 50 days.

3. Conclusion

We report a room-temperature-operating self-aligned MWIR MPM vdW heterojunction photodetector enhanced by sandwiched metal mirrors. An ultra-broadband photoresponse from 0.405 to 3.951 µm was demonstrated. A fast photoresponse τ_r = 3.1 µs and τ_d = 4.1 µs and −3 dB cutoff frequency 0.23 MHz were realized under a 1550 nm laser. The MPM photodetector exhibited a high blackbody peak photoresponsivity up to 0.77 A W^{-1}, a low noise-equivalent power of $\approx 2.0 \times 10^{-14}$ W Hz$^{-1/2}$ and a high specific detectivity up to 8.61×10^{10} cm Hz$^{1/2}$W^{-1} in the MWIR region under 1073 K blackbody radiation. An effective detection range of up to 75% was demonstrated.

4. Experimental Section

Device Fabrication: The bottom electrodes were patterned using electron-beam lithography and then electron-beam evaporation deposition of 5 nm Cr and 25 nm Au on a low resistance Si substrate with 300 nm SiO_2. Using standard mechanical exfoliation methods, MoS_2, and BP flakes were prepared and then sequentially transferred to the preprepared bottom electrode. To obtain a high-quality MPM vdW device, the thin film MoS_2 and BP flake preparation and heterostructure fabrication processes were carried out in a high-purity nitrogen-filled glove box, where there was a very low (<0.1 ppm) concentration of oxygen and water. A self-aligned metal electrode of 8 nm Bi and 2 nm Au was then evaporated using standard electron beam evaporation.

Characterization Methods: The thicknesses of the BP and MoS_2 flakes were examined by atomic force microscopy (HITACHI, AFM 5500 M). Raman spectra were measured using a 532 nm laser as an excitation source by a Renishaw invia-Reflex system. The interface of the stacked structure of the MoS_2/BP/MoS_2 vdW heterojunction was examined by field-emission TEM (JEOL, JEM-F200). The cross-section specimen was prepared using a focused ion beam system (ZEISS, crossbeam 550), and then, a thin layer of Au was coated to protect the sample.

Electrical and Photoresponse Measurements: Electrical transport measurements were carried out using a dual-channel digital source meter (Keithley 2636B). A homemade wavelength-tuneable multichannel MWIR laser (2.5–4.2 µm) was used to study the MWIR performance of the photodetector. The diameter of the MWIR laser beam was 3 mm. The laser, with a wavelength from 405 to 1550 nm, was focused on the device using a 20× objective lens. The blackbody response measurement was performed using an HFY-206A calibrated commercial blackbody source. The diameter of the aperture was 10 mm. The device was placed 15 cm from the aperture without a focusing lens. The radiation power incident on the device was calculated using the approximate formula $P_B = \alpha\varepsilon\sigma(T_B^4 - T_R^4)AR_A^2/L^2$, where α is the modulation factor, ε is the average emissivity of the blackbody radiation source and σ is the Stefan-Boltzmann constant. Here, α = 0.35 and ε = 0.9. T_B and T_R are the temperature of the blackbody source and the ambient temperature, respectively.

Supporting Information

Supporting Information is available from the Wiley Online Library or from the author.

© 2022 Wiley-VCH GmbH
15214095, 2022, 39, Downloaded from https://onlinelibrary.wiley.com/doi/10.1002/adma.202203283 by Cas-Changchun Institute Of Optics, Fine Mechanics And Physics, Wiley Online Library on [06/02/2023]. See the Terms and Conditions (https://onlinelibrary.wiley.com/terms-and-conditions) on Wiley Online Library for rules of use; OA articles are governed by the applicable Creative Commons License

15214095, 2022, 39, Downloaded from https://onlinelibrary.wiley.com/doi/10.1002/adma.202203283 by Cas-Changchun Institute Of Optics, Fine Mechanics And Physics, Wiley Online Library on [06/02/2023]. See the Terms and Conditions (https://onlinelibrary.wiley.com/terms-and-conditions) on Wiley Online Library for rules of use; OA articles are governed by the applicable Creative Commons License

Acknowledgements

This work was supported by the National Natural Science Foundation of China (Grant Nos. 61725505, 61975224, 62004207, and 12074002), University Synergy Innovation Program of Anhui Province (Grant No. GXXT-2020-050), Fund of Anhui Provincial Natural Science Foundation (Grant No. 2008085MF206), National Key R&D Program of China (Grant Nos. 2017YFA0302904, 2018YFA0305602), Shanghai Sailing Project (Grant No. 20YF1455900), Special Research Assistant Grant from the Chinese Academy of Sciences Foundation (Grant No. 2019–169), Major Basic Program of Natural Science Foundation of Shandong Province (Grant No. ZR2021ZD01), Recruitment Program for Leading Talent Team of Anhui Province, 2020, Open Fund of State Key Laboratory of Infrared Physics (Grant No. SITP-NLIST-YB-2022-06), State Key Laboratory of Luminescence and Applications (Grant No. SKLA-2021-03), Open Fund of Information Materials and Intelligent Sensing Laboratory of Anhui Province (Grant No. IMIS202101) and Open Fund of Infrared and Low-Temperature Plasma Key Laboratory of Anhui Province (Grant No. IRKL2022KF03). The authors thank professor Xiaomu Wang at Nanjing University for their experimental support and helpful discussion.

Conflict of Interest

The authors declare no conflict of interest.

Author Contributions

F.W., Z.L., and T.Z. contributed equally to this work. M.L. and W.H. conceived the project and designed the experiments. F.W., M.L., T.Z., and, Z.L., performed device fabrication. F.W., M.L., T.Z., Z.L., H.W., X.W. performed device characterization, Y.G. is responsible for electric simulation, H.G. and R.X. are responsible for optical absorption simulation. M.L., F.W., Z.L., T.Z., and W.H. performed data analysis and interpretation. M.L., F.W., J.H., and W.H. co-wrote the paper, and all authors contributed to the discussion and preparation of the manuscript.

Data Availability Statement

The data that support the findings of this study are available from the corresponding author upon reasonable request.

Keywords

2D materials, black phosphorus, molybdenum disulfide, photodetectors, van der Waals heterojunctions

Received: April 12, 2022
Revised: July 21, 2022
Published online: August 25, 2022

[1] A. M. Itsuno, J. D. Phillips, S. Velicu, *Appl. Phys. Lett.* **2012**, *100*, 161102.
[2] L. Mollard, G. Destefanis, N. Baier, J. Rothman, P. Ballet, J. P. Zanatta, M. Tchagaspanian, A. M. Papon, G. Bourgeois, J. P. Barnes, C. Pautet, P. Fougères, *J. Electron. Mater.* **2009**, *38*, 1805.
[3] A. Rogalski, *Rep. Prog. Phys.* **2005**, *68*, 2267.
[4] A. Rogalski, *J. Alloys Compd.* **2004**, *371*, 53.
[5] A. O. J. M. Manuel Pujadas, *Proc. SPIE* **1995**, *2506*, 738.
[6] H. Lee, C. Oh, J. W. Hahn, *Infrared Phys. Technol.* **2013**, *57*, 50.
[7] N. Kuze, E. G. Camargo, K. Ueno, T. Morishita, M. Sato, M. Kurihara, H. Endo, K. Ishibashi, *J. Cryst. Growth* **2007**, *301*, 997.
[8] L. Zeng, D. Wu, J. Jie, X. Ren, X. Hu, S. P. Lau, Y. Chai, Y. H. Tsang, *Adv. Mater.* **2020**, *32*, 2004412.
[9] M. Long, F. Liu, F. Ding, Y. Wang, J. Ye, R. Xie, H. Wang, M. Xu, F. Wang, Y. Tu, T. Han, F. Li, Z. Zhang, L. Liu, *Appl. Phys. Lett.* **2020**, *117*, 231104.
[10] X. Yu, Y. Li, X. Hu, D. Zhang, Y. Tao, Z. Liu, Y. He, M. A. Haque, Z. Liu, T. Wu, Q. J. Wang, *Nat. Commun.* **2018**, *9*, 4299.
[11] S. Yuan, C. Shen, B. Deng, X. Chen, Q. Guo, Y. Ma, A. Abbas, B. Liu, R. Haiges, C. Ott, T. Nilges, K. Watanabe, T. Taniguchi, O. Sinai, D. Naveh, C. Zhou, F. Xia, *Nano Lett.* **2018**, *18*, 3172.
[12] M. Long, Y. Wang, P. Wang, X. Zhou, H. Xia, C. Luo, S. Huang, G. Zhang, H. Yan, Z. Fan, X. Wu, X. Chen, W. Lu, W. Hu, *ACS Nano* **2019**, *13*, 2511.
[13] X. Zhang, C. Yan, X. Hu, Q. Dong, Z. Liu, W. Lv, C. Zeng, R. Su, Y. Wang, T. Sun, Z. Xing, C. Pang, B. Zhang, W. Shi, M. Long, *Mater. Res. Exp.* **2021**, *8*, 035602.
[14] S. Deckoff-Jones, Y. Wang, H. Lin, W. Wu, J. Hu, *ACS Photonics* **2019**, *6*, 1632.
[15] M. Dai, C. Wang, M. Ye, S. Zhu, S. Han, F. Sun, W. Chen, Y. Jin, Y. Chua, Q. J. Wang, *ACS Nano* **2022**, *16*, 295.
[16] R. J. Suess, E. Leong, J. L. Garrett, T. Zhou, R. Salem, J. N. Munday, T. E. Murphy, M. Mittendorff, *2D Mater.* **2016**, *3*, 41006.
[17] J. Na, Y. T. Lee, J. A. Lim, D. K. Hwang, G.-T. Kim, W. K. Choi, Y.-W. Song, *ACS Nano* **2014**, *8*, 11753.
[18] Y. Liu, N. O. Weiss, X. Duan, H.-C. Cheng, Y. Huang, X. Duan, *Nat. Rev. Mater.* **2016**, *1*, 16042.
[19] Y. Ma, B. Dong, J. Wei, Y. Chang, L. Huang, K.-W. Ang, C. Lee, *Adv. Opt. Mater.* **2020**, *8*, 2000337.
[20] L. Huang, B. Dong, X. Guo, Y. Chang, N. Chen, X. Huang, W. Liao, C. Zhu, H. Wang, C. Lee, K.-W. Ang, *ACS Nano* **2019**, *13*, 913.
[21] N. Youngblood, C. Chen, S. J. Koester, M. Li, *Nat. Photonics* **2015**, *9*, 247.
[22] P. K. Venuthurumilli, P. D. Ye, X. Xu, *ACS Nano* **2018**, *12*, 4861.
[23] W. Yan, V. R. Shresha, Q. Jeangros, N. S. Azar, S. Balendhran, C. Ballif, K. Crozier, J. Bullock, *ACS Nano* **2020**, *14*, 13645.
[24] Q. Guo, A. Pospischil, M. Bhuiyan, H. Jiang, H. Tian, D. Farmer, B. Deng, C. Li, S.-J. Han, H. Wang, Q. Xia, T.-P. Ma, T. Mueller, F. Xia, *Nano Lett.* **2016**, *16*, 4648.
[25] B. Liu, M. Köpf, A. N. Abbas, X. Wang, Q. Guo, Y. Jia, F. Xia, R. Weihrich, F. Bachhuber, F. Pielnhofer, H. Wang, R. Dhall, S. B. Cronin, M. Ge, X. Fang, T. Nilges, C. Zhou, *Adv. Mater.* **2015**, *27*, 4423.
[26] M. Long, A. Gao, P. Wang, H. Xia, C. Ott, C. Pan, Y. Fu, E. Liu, X. Chen, W. Lu, T. Nilges, J. Xu, X. Wang, W. Hu, F. Miao, *Sci. Adv.* **2017**, *3*, e1700589.
[27] X. Chen, X. Lu, B. Deng, O. Sinai, Y. Shao, C. Li, S. Yuan, V. Tran, K. Watanabe, T. Taniguchi, D. Naveh, L. Yang, F. Xia, *Nat. Commun.* **2017**, *8*, 1672.
[28] M. Amani, E. Regan, J. Bullock, G. H. Ahn, A. Javey, *ACS Nano* **2017**, *11*, 11724.
[29] J. Bullock, M. Amani, J. Cho, Y.-Z. Chen, G. H. Ahn, V. Adinolfi, V. R. Shrestha, Y. Gao, K. B. Crozier, Y.-L. Chueh, A. Javey, *Nat. Photonics* **2018**, *12*, 601.
[30] Y. Chen, Y. Wang, Z. Wang, Y. Gu, Y. Ye, X. Chai, J. Ye, Y. Chen, R. Xie, Y. Zhou, Z. Hu, Q. Li, L. Zhang, F. Wang, P. Wang, J. Miao, J. Wang, X. Chen, W. Lu, P. Zhou, W. Hu, *Nat. Electron.* **2021**, *4*, 357.
[31] M. Peng, R. Xie, Z. Wang, P. Wang, F. Wang, H. Ge, Y. Wang, F. Zhong, P. Wu, J. Ye, Q. Li, L. Zhang, X. Ge, Y. Ye, Y. Lei, W. Jiang, Z. Hu, F. Wu, X. Zhou, J. Miao, J. Wang, H. Yan, C. Shan, J. Dai, C. Chen, X. Chen, W. Lu, W. Hu, *Sci. Adv.* **2021**, *7*, f7358.

© 2022 Wiley-VCH GmbH

[32] P.-C. Shen, C. Su, Y. Lin, A.-S. Chou, C.-C. Cheng, J.-H. Park, M.-H. Chiu, A.-Y. Lu, H.-L. Tang, M. M. Tavakoli, G. Pitner, X. Ji, Z. Cai, N. Mao, J. Wang, V. Tung, J. Li, J. Bokor, A. Zettl, C.-I. Wu, T. Palacios, L.-J. Li, J. Kong, *Nature* **2021**, *593*, 211.
[33] L. Wang, I. Meric, P. Y. Huang, Q. Gao, Y. Gao, H. Tran, T. Taniguchi, K. Watanabe, L. M. Campos, D. A. Muller, J. Guo, P. Kim, J. Hone, K. L. Shepard, C. R. Dean, *Science* **2013**, *342*, 614.
[34] Y. Li, A. Chernikov, X. Zhang, A. Rigosi, H. M. Hill, A. M. van der Zande, D. A. Chenet, E. M. Shih, J. Hone, T. F. Heinz, *Phys. Rev. B* **2014**, *90*, 205422.
[35] A. D. Rakic, A. B. Djurisic, J. M. Elazar, M. L. Majewski, *Appl. Opt.* **1998**, *37*, 5271.
[36] T. Low, A. S. Rodin, A. Carvalho, Y. Jiang, H. Wang, F. Xia, A. H. C. Neto, *Phys. Rev. B* **2014**, *90*, 75434.
[37] M. Tamulewicz, J. Kutrowska-Girzycka, K. Gajewski, J. A. Serafi Czuk, A. Sierakowski, J. Jadczak, L. Bryja, T. P. Gotszalk, *Nanotechnology* **2019**, *30*, 245708.
[38] X. Liu, D. Qu, H.-M. Li, I. Moon, F. Ahmed, C. Kim, M. Lee, Y. Choi, J. H. Cho, J. C. Hone, W. J. Yoo, *ACS Nano* **2017**, *11*, 9143.
[39] J. Hong, K. Li, C. Jin, X. Zhang, Z. Zhang, J. Yuan, *Phys. Rev. B* **2016**, *93*, 75440.
[40] L. Li, W. Wang, L. Gan, N. Zhou, X. Zhu, Q. Zhang, H. Li, M. Tian, T. Zhai, *Adv. Funct. Mater.* **2016**, *26*, 8281.
[41] W. Zhang, J.-K. Huang, C.-H. Chen, Y.-H. Chang, Y.-J. Cheng, L.-J. Li, *Adv. Mater.* **2013**, *25*, 3456.
[42] S. Ghosh, A. Varghese, K. Thakar, S. Dhara, S. Lodha, *Nat. Commun.* **2021**, *12*, 3336.
[43] Q. Zhao, W. Wang, F. Carrascoso-Plana, W. Jie, T. Wang, A. Castellanos-Gomez, R. Frisenda, *Mater. Horiz.* **2020**, *7*, 252.
[44] M. M. Furchi, A. Pospischil, F. Libisch, J. Burgdörfer, T. Mueller, *Nano Lett.* **2014**, *14*, 4785.
[45] D. Rauh, C. Deibel, V. Dyakonov, *Adv. Funct. Mater.* **2012**, *22*, 3371.
[46] C. Soci, A. Zhang, B. Xiang, S. A. Dayeh, D. P. R. Aplin, J. Park, X. Y. Bao, Y. H. Lo, D. Wang, *Nano Lett.* **2007**, *7*, 1003.
[47] W. Zhang, C.-P. Chuu, J.-K. Huang, C.-H. Chen, M.-L. Tsai, Y.-H. Chang, C.-T. Liang, Y.-Z. Chen, Y.-L. Chueh, J.-H. He, M.-Y. Chou, L.-J. Li, *Sci. Rep.* **2014**, *4*, 3826.
[48] G. Konstantatos, M. Badioli, L. Gaudreau, J. Osmond, M. Bernechea, F. P. García De Arquer, F. Gatti, F. H. L. Koppens, *Nat. Nanotechnol.* **2012**, *7*, 363.
[49] Y. Fang, A. Armin, P. Meredith, J. Huang, *Nat. Photonics* **2019**, *13*, https://doi.org/10.1038/s41566-018-0288-z.

© 2022 Wiley-VCH GmbH

15214095, 2022, 39, Downloaded from https://onlinelibrary.wiley.com/doi/10.1002/adma.202203283 by Cas-Changchun Institute Of Optics, Fine Mechanics And Physics, Wiley Online Library on [06/02/2023]. See the Terms and Conditions (https://onlinelibrary.wiley.com/terms-and-conditions) on Wiley Online Library for rules of use; OA articles are governed by the applicable Creative Commons License